Reducing Entanglement with Physically Inspired Fermion-To-Qubit Mappings

Teodor Parella-Dilmé[ORCID],[1,*] Korbinian Kottmann[ORCID],[1] Leonardo Zambrano[ORCID],[1] Luke Mortimer[ORCID],[1]
Jakob S. Kottmann[ORCID],[2,3,†] and Antonio Acín[1,4]

[1] *ICFO—Institut de Ciencies Fotoniques, The Barcelona Institute of Science and Technology, Avinguda Carl Friedrich Gauss 3, 08860 Castelldefels, Barcelona, Spain*

[2] *Institute for Computer Science, University of Augsburg, Universitätsstraße 6a, 86159 Augsburg, Germany*

[3] *Center for Advanced Analytics and Predictive Sciences, University of Augsburg, Germany*

[4] *ICREA—Institucio Catalana de Recerca i Estudis Avancats, Lluis Companys 23, 08010 Barcelona, Barcelona, Spain*

In *ab initio* electronic structure simulations, fermion-to-qubit mappings represent the initial encoding step from the problem of fermions into a problem of qubits. This work introduces a physically inspired method for constructing mappings that significantly simplify entanglement requirements when one is simulating states of interest. The presence of electronic excitations drives the construction of our mappings, reducing correlations for target states in the qubit space. To benchmark our method, we simulate ground-states of small molecules and observe an enhanced performance when compared with classical and quantum variational approaches from prior research using conventional mappings. In particular, on the quantum side, our mappings require a reduced number of entangling layers to achieve accuracy for LiH, H_2, $(H_2)_2$, $H_4^{\neq}$ stretching, and benzene's π system using the RY hardware-efficient ansatz. In addition, our mappings also provide an enhanced ground-state simulation performance in the density matrix renormalization group algorithm for the N_2 molecule.

I. INTRODUCTION

Ab initio electronic structure simulations play a pivotal role in various fields, including drug development [1,2], computational catalysis [3], and materials science [4]. Given the significance of this domain, numerous techniques have evolved over the years, enabling simulations of increasingly complex systems. In the context of our research, it is worth mentioning three specific methods: classical simulations, variational quantum algorithms executed on current and near-term noisy quantum devices, and fault-tolerant quantum computing. Classical simulations in the form of the density matrix renormalization group (DMRG) algorithm [5–8] and Monte Carlo methods [9] are state-of-the-art methods and are readily available. Variational quantum algorithms are executed on proof-of-concept scales on contemporary noisy quantum computing devices, and have the potential for achieving simulations

of useful system sizes soon. Finally, quantum algorithms on fault-tolerant quantum computers are expected to yield useful applications in the further future when such computers are available and the gate counts and runtimes of these algorithms are reduced to practical numbers.

Central to all approaches is the transformation of the physical problem into units of information. This involves the selection of an appropriate basis consisting of a set of spin-orbitals (SOs), on top of a fermion-to-qubit mapping. In this work, we focus on the choice of fermion-to-qubit mappings, which leads to potential advantages in all three formerly mentioned avenues.

Fermion-to-qubit mappings represent the initial encoding step of fermionic problems into qubits, faithfully replicating the algebra of fermionic operators on a qubit system [10]. Given the nonlocal nature of the fermionic state space, these mappings introduce a nonlocal structure into qubit systems, which are typically characterized by a limited connectivity. It is crucial to emphasize that these mappings are not unique, as there are numerous possible solutions to the encoding problem. Consequently, depending on the qubit topology and the technique applied, some mappings may prove more advantageous than others for simulation tasks. In this context, the reduction of Pauli weight, locality of mapped operators, entangling gate overhead, and number of qubits has played a leading role in

---

the design of novel mappings, all while one considers the practical constraints imposed by experimental hardware [11–18]. Here we follow a different path and choose entanglement as the relevant figure of merit: our goal is to design fermion-to-qubit mappings that reduce the entanglement in the target qubit state.

Given an initial fermionic Hamiltonian, its energy spectrum remains invariant under any valid fermion-to-qubit transformation. However, the eigenstates of the resulting qubit Hamiltonian, and consequently the target state $|\psi\rangle$ to be simulated, differ across the mappings. In particular, the target state can exhibit substantial variations in its entanglement properties in a qubit representation, which is a critical factor influencing the quality of the simulations, both in the classical case and in the quantum case. For instance, it is not clear if the Pauli weight has any impact on DMRG simulations, while they are known to be affected by the entanglement structure of the target state. In general, identification of mappings yielding states with reduced entanglement requirements could substantially enhance simulation performance.

In this work, a physically inspired method is proposed to construct tailored entanglement-aware fermion-to-qubit mappings with reduced entanglement requirements on the state being simulated. For small molecular systems, we show enhanced ground-state preparation performance with respect to paradigmatic mappings. In the quantum computation framework, we use the variational quantum eigensolver (VQE) with an RY hardware-efficient ansatz (HEA) to demonstrate increased accuracy for LiH, H_2, $(H_2)_2$, $H_4^{\neq}$ stretching, and benzene's π system. Additionally, we extend the applicability of our method to the tensor network framework, where we simulate N_2 using the DMRG on a matrix product state (MPS) representation.

II. FERMION-TO-QUBIT MAPPINGS

The problem of designing beneficial qubit representations of electronic systems is rich and can be tackled from different angles. As already mentioned, in this work we are focusing on the fermion-to-qubit mapping alone. Other studies have used different strategies to reach this goal, such as optimizing the spatial orbitals [19–21] or regularizing the electronic Hamiltonian [22–28], as well as other strategies [29–32]. Note that these are separate strategies that can be combined with optimized fermion-to-qubit mappings.

The proposed mappings can be related to recent studies aiming to find optimal Clifford circuits for entanglement reduction [33–35]. These studies can be interpreted as finding a beneficial mapping through a transformation included in the quantum circuit, while in this work we aim to find a suitable mapping directly. Our results therefore apply to both classical and quantum approaches.

A. Fock space to qubits

The antisymmetrized Fock space $\mathcal{F}_-$ encompasses all conceivable states from a many-body fermionic system. In electronic structure problems, solving for the spectrum of an operator $\hat{O} \in \mathrm{Lin}[\mathcal{F}_-]$ has significant importance, a particular case being the electronic Hamiltonian. The fermionic algebra consists of a set of creation $\{a_i^\dagger\}_{i=1}^n$ and annihilation $\{a_i\}_{i=1}^n$ operators in $\mathrm{Lin}[\mathcal{F}_-]$, satisfying canonical anticommutation relations (CARs):

$$\{a_i^\dagger, a_j\} = \delta_{ij}\mathbb{1}, \quad \{a_i, a_j\} = \{a_i^\dagger, a_j^\dagger\} = 0. \tag{1}$$

When applied to the fermionic vacuum $|vac\rangle$, such ladder operators define the orthonormal Fock basis spanning $\mathcal{F}_-$, in the so-called occupation number vector notation:

$$|f_1, f_2, \ldots, f_n\rangle \equiv (a_1^\dagger)^{f_1}(a_2^\dagger)^{f_2}\cdots(a_n^\dagger)^{f_n}|vac\rangle. \tag{2}$$

Here, $f_i \in \{0, 1\}$ is called the "fermionic occupation of mode i," $(a_i^\dagger)^0 \equiv \mathbb{1}$, and n is the total number of fermionic modes available. Note that the ladder operators are applied in descending order, as a phase factor could apply otherwise. Equivalently, ladder operators can be decomposed as

$$a_j = \frac{1}{2}(\gamma_{2j} + i\gamma_{2j-1}), \quad a_j^\dagger = \frac{1}{2}(\gamma_{2j} - i\gamma_{2j-1}) \tag{3}$$

into a self-adjoint part (γ_{2j}) and an anti-self-adjoint part $(i\gamma_{2j-1})$. They are uniquely identified by a Majorana basis $\{\gamma_j\}_{j=1}^{2d}$, satisfying both being self-adjoint $(\gamma_j = \gamma_j^\dagger)$ and the associated CAR for Majorana operators

$$\{\gamma_j, \gamma_k\} = 2\delta_{jk}\mathbb{1}. \tag{4}$$

Operators in $\mathrm{Lin}[\mathcal{F}_-]$ can be expressed as linear combinations of products of a set of ladder operators. In particular, the electronic Hamiltonian is expressed as a linear combination of one-body and two-body operators as

$$\hat{H}_e = \sum_{i,j} h_{ij}\hat{a}_i^\dagger\hat{a}_j + \sum_{i,j,k,l} h_{ijkl}\hat{a}_i^\dagger\hat{a}_j^\dagger\hat{a}_l\hat{a}_k, \tag{5}$$

with h_{ij} and h_{ijkl} being the one-body and two-body terms, respectively, available from classical computation methods.

The abstract Fock space spanned by n fermionic modes is isomorphic to the Hilbert space spanned by n qubits $\mathcal{F}_- \simeq (\mathbb{C}^2)^{\otimes n}$, with dimension 2^n. Hence, it is always possible to transform the Fock space to a qubit space through a so-called fermion-to-qubit mapping:

$$\Lambda : \quad \mathcal{F}_- \rightarrow (\mathbb{C}^2)^{\otimes n}. \tag{6}$$

These mappings also transform ladder operators into operators in $\mathrm{Lin}[\mathcal{F}_-]$ satisfying the CAR. After application of any such mappings, any electronic Hamiltonian $\hat{H}_e$ is fully reconstructed in the qubit space.

B. Ternary tree encodings

The relation between ternary trees (TTs) and mappings was introduced in Ref. [11]. In Ref. [12], a TT mapping was proven to be optimal to minimize the Pauli weight of the derived operators in $\text{Lin}[\mathcal{F}_-]$. This ignited the research reported in Ref. [18], where the flexibility of generating TT mappings was implemented favorably on experimental hardware. Moreover, Ref. [18] includes a thorough discussion on TT mappings, a detailed pairing scheme preserving a fermionic vacuum, and analysis of occupation localization. Overall, the TT formalism provides a large framework of fermion-to-qubit mappings based on Pauli strings, including the representation of traditional mappings such as Jordan-Wigner (JW) [36], parity, and Fenwick tree–based mappings such as Bravyi-Kitaev mapping [10]. Such a TT formalism enables the retrieval of a Majorana basis set in the qubit representation from a TT, satisfying Eq. (4).

We briefly introduce a TT as a graph $\mathcal{T} = (V, E)$ consisting of a set of m vertices $V = \{v_i\}_{i=1}^m$ and $(m-1)$ connecting edges $E \subseteq \{(x, y) \in V^2 | x \neq y\}$ (Fig. 1). In the upper part of the TT, there is the root node, which ramifies the graph iteratively up to three labeled descendants per node. For two connected nodes v_i, v_j, a kinship relationship is set between them. With respect to v_i, the node v_j can take the relationship of parent (v_i^p), x child (v_i^x), y child (v_i^y), or z child (v_i^z). The same applies for v_i. Except for the root node (which has no parent), every node has one and only one associated parent, and up to three labeled children. If a node is missing some x, y, or z child, then for each missing child a leg from the ternary tree is defined. Formally, a "leg" refers to an edge that is connected to a single graph node, with no connection at its other end. In total, there are $2m + 1$ resulting legs on the ternary tree. Each leg l has an associated Pauli string S_l (Table I), which

can be retrieved by one tracing the ascending path back to the root node. Initially, the node v_i on top of the current leg x, y or z denotes respectively an X, Y or Z Pauli operator to be applied to the ith qubit. Subsequently, as we progress to the parent node $v_j = v_i^p$, the relationship between v_i and v_j delineates v_j^x, v_j^y or v_j^z, signifying respectively an X, Y or Z Pauli operator to be applied to the jth qubit. By our redefining $v_i \equiv v_i^p$, the process is repeated iteratively, where each iteration retrieves the operators to be applied to each parent node. In the final step, v_i^p becomes the root node of the ternary tree, having no associated parents, and terminating the process. The associated Pauli string S_l for leg l results from tensoring the Pauli operators of the aforementioned progression. The resulting set of Pauli strings from the TT are defined as Majorana strings ($S_l = S_l^\dagger$). These replicate the fermionic CAR for Majorana operators from Eq. (4) in qubit space. Ultimately, the Majorana strings may be paired to preserve the fermionic vacuum through the pairing algorithm (Algorithm 2).

For further details about the TT formalism, we refer the reader to the detailed explanations in Refs. [11,18]. In this work, the TT formalism was implemented with use of the TEQUILA [37] PYTHON library.

C. Fermionic permutation and qubit permutation

In this section, we discuss a fundamental yet often misunderstood distinction between fermionic permutation and qubit permutation. The former refers to the relative permutation of fermionic modes encoded within the TT mapping, directly affecting the transformation and further simulation requirements [38]. The latter involves a reordering of qubits, leaving the transformation intact but having significant implications when one is conducting simulations with algorithms or devices with restricted topologies. To ensure clarity, we elaborate on the distinction between both permutations through explicit and illustrative examples.

We draw special attention to the resulting effects of encoding parity locally. In the literature, parity mappings are often referred to as a unique parity mapping. However, the specific order in which the fermionic occupation is encoded results in nonequivalent mappings.

Encoding locally in parity involves encoding in either the x branch or the y branch of a ternary tree. To simplify our discussion, we focus on the former case and consider an x-branch mapping of four fermionic modes labeled "0," "1," "2," and "3" onto four qubits labeled "A," "B," "C," and "D" in standard order [Fig. 2(a)]. We explore another x-branch parity mapping where modes are encoded in the order 1, 3, 0, 2 [Fig. 2(b)]. Lastly, we present the JW mapping in the standard order for the purpose of comparison [Fig. 2(c)].

The fermionic modes held by each node from the tree do have relevant implications for the mapping, and lead to different fermion-to-qubit mappings. We say that the
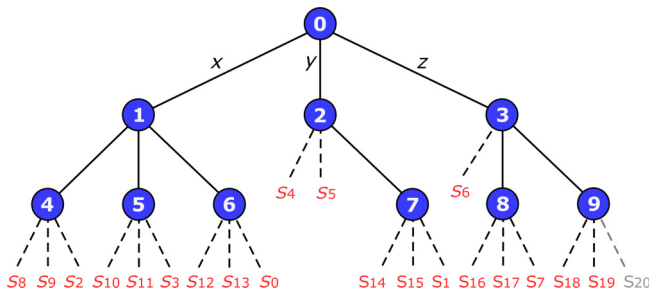

FIG. 1. Ternary tree example, corresponding to a fermion-to-qubit mapping of ten fermionic modes. Each node holds a fermionic mode, an ascending parent node (except from the root node at the top), and three descending labeled branches x, y, z (from left to right, respectively) indicating the child nodes. The dashed lines correspond to legs of the tree, each retrieving a single Majorana string S_i in red. The leg associated with z paths forming the root node is marked in gray, and its Majorana string is unpaired.
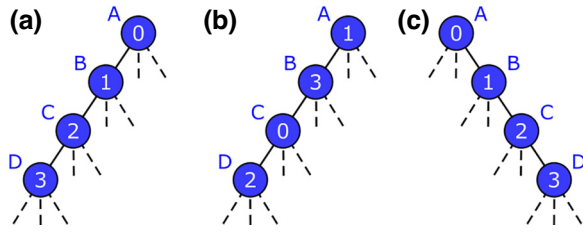
FIG. 2. Ternary trees of fermion-to-qubit encodings with four fermionic modes (0, 1 ,2, and 3) into four qubits (A, B, C, and D). (a) Parity encoding of fermions in standard order (0, 1, 2, 3). (b) Parity encoding of permuted fermions in order 1, 3, 0, 2. (c) JW encoding in standard order.

two parity mappings presented differ due to a permutation in the fermionic space. For the first mapping [Fig. 2(a)], qubit D holds the occupation of fermionic mode 3, qubit C holds the total occupation sum modulo 2 of modes 2 and 3, qubit B holds the total occupation sum modulo 2 of modes 1, 2, and 3, and qubit A holds the total occupation sum modulo 2 of all four modes. However, in the case of the second mapping [Fig. 2(b)], qubit D holds the occupation of fermionic mode 2, qubit C holds the occupation modulo 2 of modes 0 and 2, qubit B holds the occupation modulo 2 of modes 3, 0, and 2, and qubit A holds the occupation modulo 2 of all four modes. Both mappings have qubits that encode different occupation information from any other qubit in the other mapping. For instance, in the first mapping, there is a qubit holding occupation information from mode 3, or a qubit holding occupation modulo 2 of modes 2 and 3. However, in the second parity mapping, there are no such qubits; instead they are different. They are essentially nonequivalent fermion-to-qubit mappings, leading to alternative representations of the Fock space in the qubit space.

On top of this fermionic permutation that changes the mapping, one can define the physical qubit permutation, related to the relative order of qubits A, B, C, and D. Such physical permutation matters when the order of entangled subparties is relevant within an optimization method. For instance, physical permutation is important within a VQE optimization in a device with restricted qubit connectivity, or in a specific topological decomposition of a tensor (such as in a linear MPS). We remark that the physical permutation does not modify the representation of a state, but it has implications for optimization methods with finite resources.

III. SIMPLIFYING ENTANGLEMENT BY ENCODING OCCUPATION NONLOCALLY

The study of many-body electronic ground-states involves dealing with complex correlations. Typically, a Hartree-Fock (HF) self-consistent field approach is used in the first instance to identify an optimized separable

state. However, to account for correlations, it is essential to consider electronic excitations, which entail promoting electrons from occupied SOs to virtual ones. Currently, widely used methods such as configuration interaction (CI) [39] and coupled cluster [40] methods aim to represent these excitations through parameterizations. The principle remains similar in its unitary variant [unitary coupled cluster (UCC)] (see Sec. IV) [41].

In this section, we propose an approach to streamline the treatment of correlations during the fermion-to-qubit encoding process. To illustrate this idea, we initially examine idealized fermionic scenarios involving pure states.

A. Double electronic excitation

We first consider a scenario involving four SOs related to a generalized double excitation, which corresponds to the simultaneous promotion of two electrons from two occupied fermionic modes to two unoccupied ones. An example is a simultaneous promotion of two electrons occupying the two SOs from the same molecular orbital (MO) to the two SOs from a virtual MO. In the context of the JW encoding [Fig. 2(c)], the occupation information for the initially filled fermionic modes 0 and 1 is locally encoded in qubits A and B, respectively. Similarly, the occupation of the two virtual fermionic modes 2 and 3 is locally encoded in qubits C and D, respectively. In this context, the state resulting from the double excitation is represented as follows:

$$|\psi\rangle^{\text{JW}}_{ABCD} = \alpha|1100\rangle^{\text{JW}}_{ABCD} + \beta|0011\rangle^{\text{JW}}_{ABCD}. \qquad (7)$$

An alternative approach may be explored by one encoding locally in parity. We call P the parity mapping from Fig. 2(a), where qubits A, B, C, and D hold, respectively, the occupation modulo 2 of the last four, three, two, and

ALGORITHM 1. Algorithm used in this work to find reduced-entanglement fermion-to-qubit mappings.

Require: A Hartree-Fock $|\psi_{HF}\rangle$ approximation of the target state in JW encoding, and a decision protocol $\mathcal{D}$ to select the relevant excitations from UpCCGSD analysis.

1: Compute UpCCGSD optimization over $|\psi_{HF}\rangle$.
2: Retrieve the absolute values for the converged angles $\{|\theta^s_{i,j}|, |\theta^d_{i,j}|\}_{i,j}$.
3: Through the decision protocol $\mathcal{D}$, select relevant excitation/s with large value/s of $\{|\theta^s_{i,j}|, |\theta^d_{i,j}|\}_{i,j}$, involving modes with relevant electronic occupation.
4: For each selected excitation, encode the associated fermionic modes in a x-branch of a TT mapping $\mathcal{T}$, replicating Eqs.(10, 14).
5: Complete $\mathcal{T}$ by encoding the remaining fermionic modes occupation locally in the qubits. This is achieved by stemming a z-branch from the root node.
6: **return** A tailored mapping $\mathcal{T}$ having the target state representation with reduced entanglement requirements.
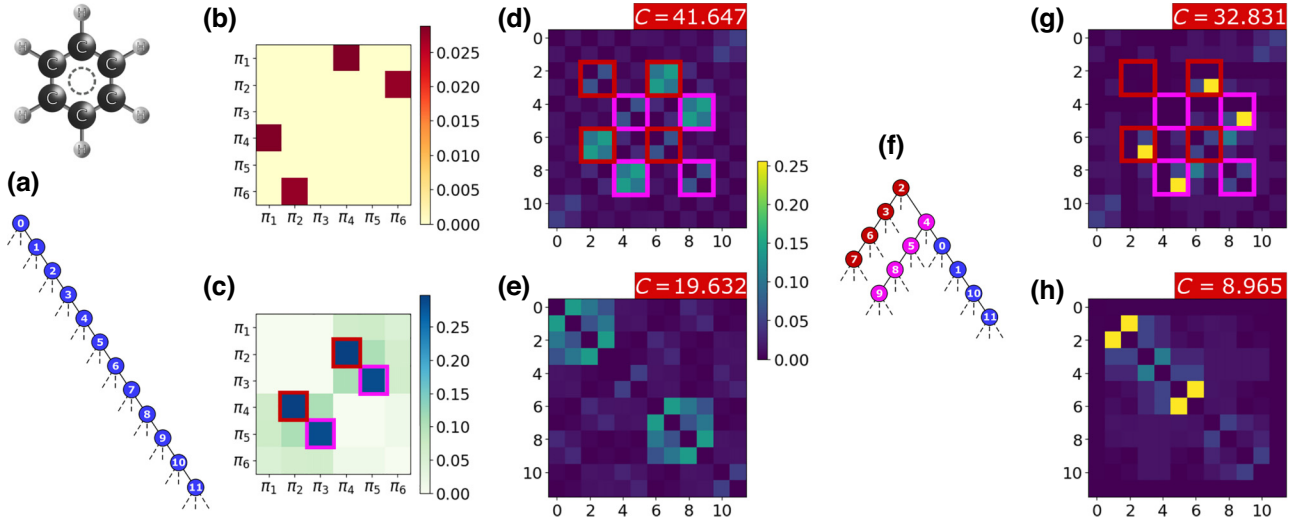

FIG. 3.   Simplification of correlations for the six MOs involved in the π system of benzene (Fig. 7). Red labels indicate the cost function value from Eq. (16) of the corresponding mutual information matrices. Red and pink squares indicate the elements associated with the most relevant double excitations. (a) TT corresponding to JW encoding. (b) Absolute values $|\theta_{ij}^s|$ after UpCCGSD, corresponding to single excitations between MOs π_i and π_j. (c) Absolute values $|\theta_{ij}^d|$ after UpCCGSD, corresponding to double excitations between MOs π_i and π_j. (d) Mutual information matrix between qubits for the JW exact ground-state. (e) Reordered mutual information matrix minimizing the correlation cost function C (final value shown). (f) Constructed mapping encoding the most relevant double excitation subspaces locally in parity. (g) Exact ground-state mutual information matrix for the adapted mapping that reduces entanglement on the double excitations between qubits 2, 3, 6, and 7 and qubits 4, 5, 8, and 9. (h) Reordered mutual information matrix for the adapted mapping.

one fermionic modes. The basis elements from the JW transformation

$$\{|1100\rangle_{ABCD}^{\mathrm{JW}}, |0011\rangle_{ABCD}^{\mathrm{JW}}\} \tag{8}$$

are, under the encoding P, represented as

$$\{|0100\rangle_{ABCD}^{P}, |0001\rangle_{ABCD}^{P}\}. \tag{9}$$

That is, the parity map goes from left to right, encoding the occupation modulo 2 of the qubits on the right in the JW encoding. Ultimately, the doubly excited state in Eq. (7) transformed from the JW encoding to the P encoding is expressed as

$$\begin{aligned}|\psi\rangle_{ABCD}^{P} &= \alpha|0100\rangle_{ABCD}^{P} + \beta|0001\rangle_{ABCD}^{P} = \\ &= |00\rangle_{AC}^{P} \otimes \left(\alpha|10\rangle_{BD}^{P} + \beta|01\rangle_{BD}^{P}\right).\end{aligned} \tag{10}$$

The entangled double-excitation subspace in the JW representation involving four qubits from Eq. (7) is effectively reduced to two entangled qubits in Eq. (10) with use of the P encoding.

B. Single electronic excitation

Although double excitations represent the major source of correlations in electronic structure problems, it is worth investigating the single electronic excitation case, involving the promotion of a single electron. The resulting state

is symmetric in terms of spin, and single excitations may be computed between two MOs, involving a total of four SOs.

We explore this concept further by introducing an idealized scenario that revolves around the excitation subspace in the JW representation [Fig. 2(c)]. To better understand this, we take the state $|1100\rangle_{ABCD}$ and possible single excitations acting on it symmetrically in terms of spin. The resulting subspace is then spanned by $|1100\rangle_{ABCD}$, $|0110\rangle_{ABCD}$, and $|1001\rangle_{ABCD}$. This implies that the state can be represented as follows:

$$|\psi\rangle_{ABCD}^{\mathrm{JW}} = \alpha|1100\rangle_{ABCD}^{\mathrm{JW}} + \beta|0110\rangle_{ABCD}^{\mathrm{JW}} + \beta|1001\rangle_{ABCD}^{\mathrm{JW}}. \tag{11}$$

On closer examination, the single excitation seems to be more intricate than initially expected, involving entanglement among all four qubits. We can consider again the mapping P from Fig. 2(a). The basis elements

$$\{|1100\rangle_{ABCD}^{\mathrm{JW}}, |0110\rangle_{ABCD}^{\mathrm{JW}}, |1001\rangle_{ABCD}^{\mathrm{JW}}\} \tag{12}$$

are transformed, respectively, into

$$\{|0100\rangle_{ABCD}^{P}, |0010\rangle_{ABCD}^{P}, |0110\rangle_{ABCD}^{P}\}. \tag{13}$$
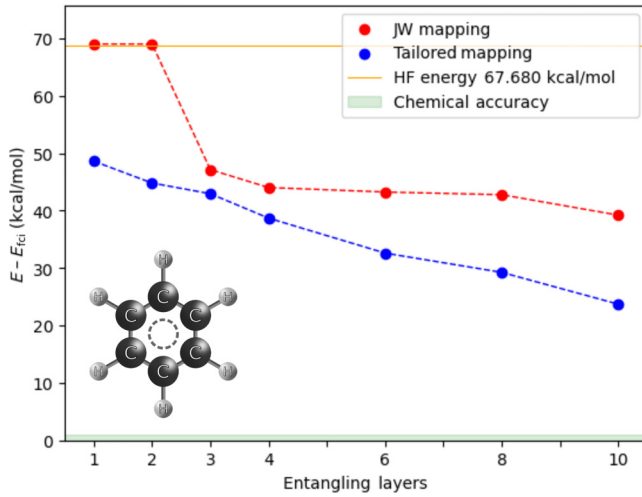
FIG. 4. $E_{\mathrm{VQE}} - E_{\mathrm{FCI}}$ as function of the RY-HEA entangling layers for the π molecular orbital subsystem of benzene. Comparison of the JW mapping (red) and tailored mapping (blue).

The singly excited state from Eq. (11) in the JW representation is transformed in the P representation to

$$|\psi\rangle^P_{ABCD} = |00\rangle^P_{AD} \otimes \left(\alpha|10\rangle^P_{BC} + \beta|01\rangle^P_{BC} + \beta|11\rangle^P_{BC}\right).$$
(14)

Most importantly, the requirement of entangling four qubits in the JW encoding for Eq. (11) is again reduced to entangling two qubits in the P encoding for Eq. (14).

Note that we used a CI-like scenario in the previous example, where a potential single electron excitation acts linearly on the initial state $|1100\rangle^{\mathrm{JW}}_{ABCD}$. In a typical quantum computing scenario, the single excitations will be introduced via a unitary coupled cluster–type operator (see the next section) that will also produce the state $|0011\rangle^{\mathrm{JW}}_{ABCD}$ where both single electrons are excited at the same time. The corresponding amplitude will be on the order of $\alpha\beta$, so the effect of the now imperfect compression under the parity mapping will become negligible for small amplitudes. As single electron excitations can be identified with orbital rotations [see Eq. (12) in Ref. [42]] this provides motivation for future combinations with orbital optimization techniques.

In complex quantum chemistry scenarios with multiple SOs and correlations, the reduced density matrices may exhibit a high degree of mixed states. This arises from the possibility of multiple excitations affecting the same SOs, thereby introducing complexity in the previously idealized cases, even in a potential orbital-optimized variant. Although we are constrained in the number of excitations we can simplify using the aforementioned methods, we can still deal with excitations that contribute the most to correlation effects.

In the following sections, our focus is on identifying relevant excitations and exploring how the entanglement

map transforms under the fermion-to-qubit mapping chosen. Our objective is to investigate the potential to mitigate correlations by using a clever mapping strategy in complex scenarios.

IV. REDUCING ENTANGLEMENT ON SMALL MOLECULAR SYSTEMS

To simplify qubit space entanglement as outlined in the previous section, we first identify the primary sources of correlation based on single and/or double excitations. Then we replicate the entanglement streamline procedure by locally encoding the parity of the fermionic modes associated with the selected excitation(s). To achieve these objectives, the algorithmic steps implemented in this work are detailed in Algorithm 1.

For clarity, we provide a detailed implementation of Algorithm 1 along with the illustrative example of benzene's π system (Fig. 7). We depart from the associated Hartree-Fock uncorrelated reference state $|\psi_{\mathrm{HF}}\rangle$ in the STO-3G basis (Table II), computed in JW encoding [Fig. 3(a)]. In this scenario, the π system is represented within an active space of six electrons, occupying the lowest-energy MOs π_1, π_2, and π_3 in the HF state. Our initial objective is to identify the most relevant electronic excitations, a task that can be accomplished through an initial simulation using reduced resources. This can be
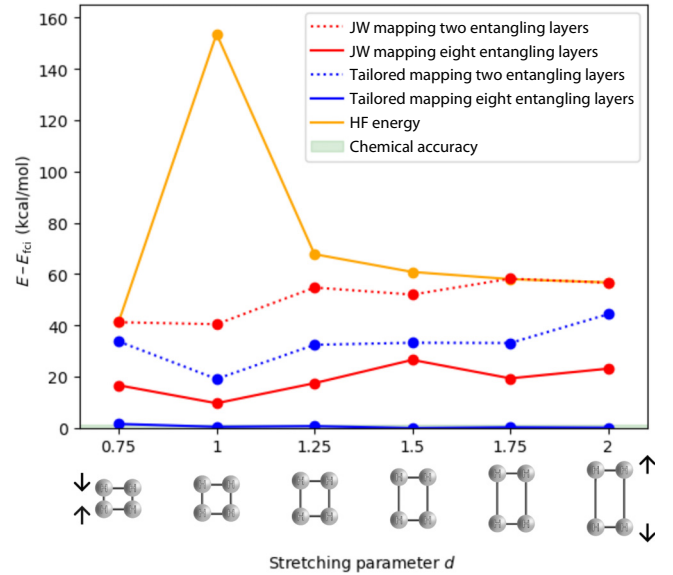

FIG. 5. Difference between E_{VQE} and E_{FCI} as a function of the stretching parameter d in the stretching of the $\mathrm{H}_4^{\neq}$ Paldus system. A comparison is made between VQE results for JW mapping (red) and tailored mapping (blue). Results are shown for the VQE RY HEA with two entangling layers (dotted lines) and eight entangling layers (solid lines). The tailored mappings used for each stretching parameter d are depicted in Fig. 12.
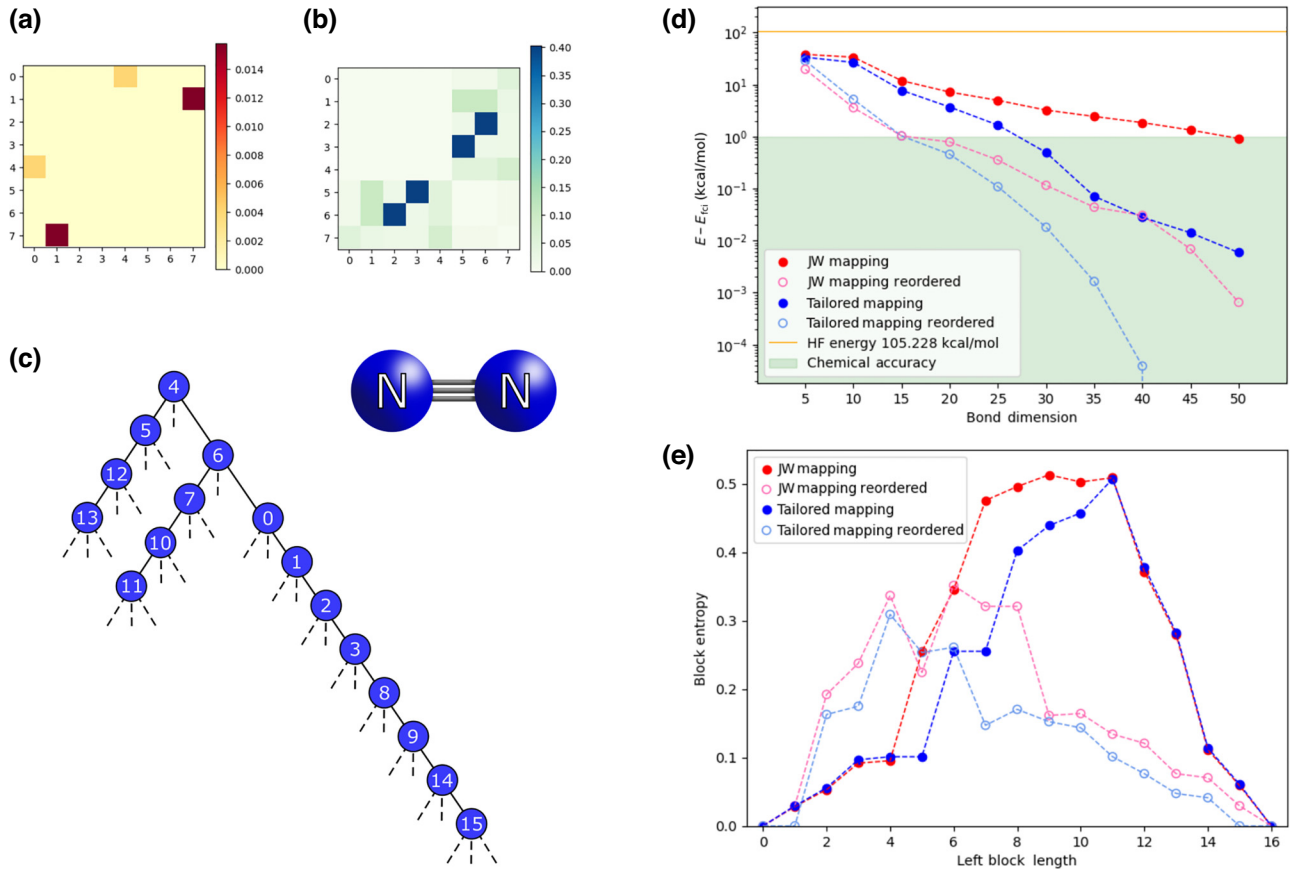
FIG. 6. DMRG results for the nitrogen molecule. (a) UpCCGSD single excitation angles between MOs for JW mapping. (b) UpCCGSD double excitation angles between MOs for JW mapping. (c) Proposed TT mapping, encoding locally in parity the spin-orbitals associated with the two double excitation subspaces (4, 5, 12, 13) and (6, 7, 10, 11). (d) Converged E_{DMRG} compared with E_{FCI} as a function of the maximum bond dimension used. The proposed TT mapping is compared with the JW mapping. The converged energy for the reordered MPS is also plotted for both mappings. (e) Block entropies for the converged MPS after use of the DMRG.

achieved through various approaches, including classical computational methods or the computation of the commutator of the corresponding operators with the Hamiltonian. A notable example of the latter is used in the building of the ansatz in the adaptive derivative-assembled pseudo-Trotter VQE [43]. Additionally, coupled cluster methods can be used, which are versatile and can be implemented with the use of classical or quantum computing techniques. In this work, we proceed with the unitary coupled cluster of singles and doubles (UCCSD), consisting in an optimization of the following parameterized state:

$$|\psi_{\text{UCCSD}}\rangle = e^{\hat{T}_1 + \hat{T}_2}|\psi_{\text{HF}}\rangle$$

$$\hat{T}_1 = \sum_{ka} \theta_{ka} \left(a_a^\dagger a_k - a_k^\dagger a_a \right)$$

$$\hat{T}_2 = \sum_{klab} \theta_{klab} \left(a_a^\dagger a_b^\dagger a_k a_l - a_k^\dagger a_l^\dagger a_a a_b \right),$$

$$(15)$$

where indices k and l represent occupied fermionic modes and indices a and b represent unoccupied ones. More

specifically, we consider the paired generalized version (UpCCGSD) [44], which considers only double excitations promoting two electrons from two filled modes of the same MO into two other modes of another virtual MO. Additionally, single excitations are considered only between modes of equal spin, being equivalent between different spin orientations of the same MOs. From now on, we define the parameterized angles θ_{ij}^s and θ_{ij}^d, respectively, as the ones involved in the single and double excitations between MOs π_i and π_j. Following the UpCCGSD analysis, we can identify relevant excitations by examining the absolute values of the optimized angles $\{|\theta_{ij}^s|\}$ and $\{|\theta_{ij}^d|\}$ for single excitations [Fig. 3(b)] and double excitations [Fig. 3(c)], respectively.

In Fig. 3(c) it is clear that there exist two critical double electronic excitations. The first one (marked by a red square) involves MOs π_2 and π_4, while the second one (marked by a pink square) involves MOs π_3 and π_5. Although there exist mild single electron excitations in Fig. 3(b), the large absolute values from double excitations are more significant.

ALGORITHM 2.   Pairing algorithm for Majorana strings from a ternary tree. Adapted from Ref. [18].

Require: A ternary Tree $\mathcal{T} = (V, E)$.
  1: **for** $v_i \in V$ **do**
  2:     **if** v_i^x is *None* **then**   ▷ Construction of S_i^x
  3:        Define l as the x-downward leg from v_i
  4:        $S_i^x \equiv S_l$
  5:     **else**
  6:        $s = v_i^x$
  7:        **while** s^z is not None **do**
  8:           $s = s^z$
  9:        Define l as the z-downward leg from s
10:        $S_i^x \equiv S_l$
11:     **if** v_i^y is *None* **then**   ▷ Construction of S_i^y
12:        Define l as the y-downward leg from v_i
13:        $S_i^y \equiv S_l$
14:     **else**
15:        $u = v_i^y$
16:        **while** u^z is not None **do**
17:           $u = u^z$
18:        Define l as the z-downward leg from u
19:        $S_i^y \equiv S_l$
20: **return** $\{S_i^x, S_i^y\}_i$ ▷ Paired Majorana strings of
21:                             all nodes v_i

It is important to mention that the following process is scalable and does not require any exact diagonalization. However, when considering small molecules as in the present case, we have the privilege of accessing the exact ground-state. As part of our analysis, and to illustrate how our approach simplifies the correlation structure, we compute the mutual information (MI) matrix, denoted as I, holding as elements I_{ij} the MI between qubits i and j. This matrix serves as a quantitative indicator of the correlation between SOs i and j [Fig. 8(d)]. An immediate observation reveals the influence of the double excitation between MO π_2 and MO π_4, as predicted above, as relevant MI is present between associated qubits 2, 3, 6, and 7 (subspace marked by red squares). The relevant double excitation between MOs π_3 and π_5 is also noticed as high correlation between associated qubits 4, 5, 8, and 9 (subspace marked by pink squares).

To streamline the state preparation process, the extent of long-range entanglement among the qubits can be minimized. This can be done by different means, such as minimizing the long-range MI between subparties [45], or through the exchange matrix [46]. Following the orbital-reordering DMRG approach in the former case, we consider the cost function on our MI matrix

$$C(I) = \sum_{i,j > i} I_{ij} |i - j|^2, \tag{16}$$

which relates to the Fiedler vector of the MI graph. In essence, the cost function tends to decrease when qubits with substantial MI are positioned closer to each other in a linear order. Considering the set of permutations of n elements $\{P\} \in \mathcal{S}_n$, the permutation P_{opt} is defined as the one that leads to an MI matrix minimizing Eq. (16):

$$P_{\text{opt}} = \arg \min_{P \in \mathcal{S}_m} C(PIP^{-1}). \tag{17}$$

As discussed in Sec. II, it is important to note that permuting physically the qubits does not alter the ground-state

TABLE I.   Explicit Pauli strings from the ternary tree in Fig. 1.

Label	Pauli string	Ternary tree
S_0	$X_0 Z_1 Z_6$	
S_1	$Y_0 Z_2 Z_7$	
S_2	$X_0 X_1 Z_4$	
S_3	$X_0 Y_1 Z_5$	
S_4	$Y_0 X_2$	
S_5	$Y_0 Y_2$	
S_6	$Z_0 X_3$	
S_7	$Z_0 Y_3 Z_8$	
S_8	$X_0 X_1 X_4$	
S_9	$X_0 X_1 Y_4$	
S_{10}	$X_0 Y_1 X_5$	
S_{11}	$X_0 Y_1 Y_5$	
S_{12}	$X_0 Z_1 X_6$	
S_{13}	$X_0 Z_1 Y_6$	
S_{14}	$Y_0 Z_2 X_7$	
S_{15}	$Y_0 Z_2 Y_7$	
S_{16}	$Z_0 Y_3 X_8$	
S_{17}	$Z_0 Y_3 Y_8$	
S_{18}	$Z_0 Z_3 X_9$	
S_{19}	$Z_0 Z_3 Y_9$	
S_{20}	$Z_0 Z_3 Z_9$	

TABLE II.   Initialization of molecular systems, including their nuclei Cartesian geometry, basis set, number of core orbitals frozen and correlation energy.

Molecule	Basis	Frozen orbitals	E^{corr}(kcal/mol)	Cartesian geometry (Å)
H_2	6-31G	0	15.4945	H 0.0000 0.0000 −0.3650
				H 0.0000 0.0000 0.3641
LiH	STO-3G	1	12.1869	Li 0.0000 0.0000 0.0000
				H 0.0000 0.0000 1.5472
$(H_2)_2$	STO-3G	0	25.4776	H 0.0000 0.3674 −2.1264
				H 0.0000 −0.3674 − 2.1264
				H 0.0000 0.0000 1.7590
				H 0.0000 0.0000 2.4939
$H_4^{\neq}(p)$	STO-3G	0	153.6310 ($d = 1$)	H 0.5601 0.5601d 0.0000
				H −0.5601 0.5601d 0.0000
				H −0.5601 − 0.5601d 0.0000
				H 0.5601 −0.5601d 0.0000
N_2	STO-3G	2	105.2284	N 0.0000 0.0000 −0.5669
				N 0.0000 0.0000 0.5669
C_6H_6	STO-3G	6	π active space: 67.6796	C 0.0000 1.4027 0.0000
				C −1.2148 0.7014 0.0000
				C −1.2148 − 0.7014 0.0000
				C 0.0000 −1.4027 0.0000
				C 1.2148 −0.7014 0.0000
				C 1.2148 0.7014 0.0000
				H 0.0000 2.4901 0.0000
				H −2.1567 1.2451 0.0000
				H −2.1567 − 1.2451 0.0000
				H 0.0000 −2.4901 0.0000
				H 2.1567 −1.2451 0.0000
				H 2.1567 1.2451 0.0000

itself but does affect the geometric constraints between subparties, which is crucial for upcoming optimization methods. 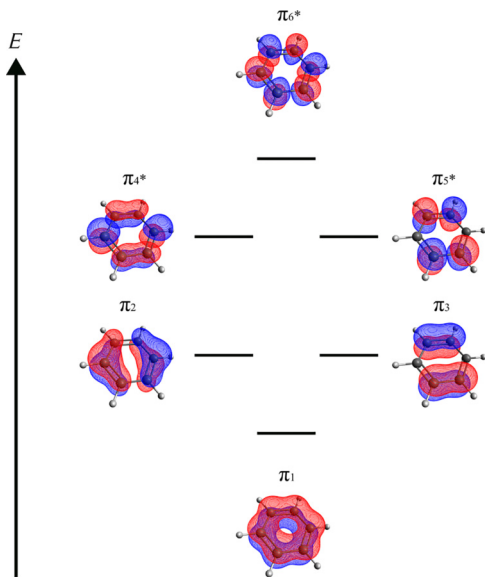Although finding the exact P_{opt} is hard, it is a good approximation P_s reducing the cost function from Eq. (16) as much as possible is sufficient. The search for P_s has demonstrated remarkable benefits in improving VQE simulations, especially on hardware with a linear restricted entangling connectivity [47]. Moreover, DMRG optimization over an MPS has also shown enhanced performance [45]. For the present case, we set P_s as the best solution found with a genetic algorithm using DEAP [48]. The reordered MI matrix associated with P_s significantly reduces the cost function (16), as shown in Fig. 3(e).

After identifying the qubits involved in the most relevant double excitations of the system [Fig. 3(c)], we proceed to transform the four-qubit entangled subspaces resulting from the double excitations described in Eq. (7) into two-qubit entangled subspaces, as described in Eq. (10). To do so, we introduce the ternary tree from Fig. 3(f), in which we have taken a decision protocol $\mathcal{D}$ that selects the modes associated with the most relevant excitations present in the UpCCGSD analysis. The qubits associated with the red (pink) double excitation are included in the red (pink) x branch. Such tailored transformation encodes occupation nonlocally between the qubits involved in each x branch (similar to a parity mapping), while occupation remains locally encoded in the qubits from the z branch (similar to JW mapping).
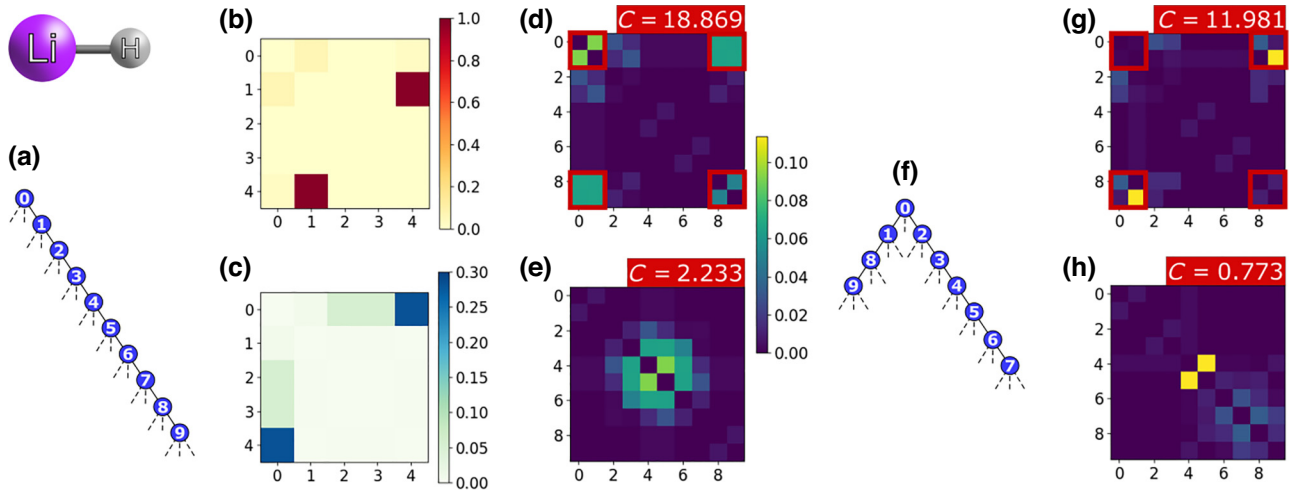

FIG. 7.   Active space of π molecular orbitals of benzene, expressed in the basis of canonical orbitals.

FIG. 8. Simplification of LiH entanglement spectrum on a five-MO active space with two electrons. Analogous to the benzene π system in Fig. 3. An analysis in the JW encoding is performed in the first instance. The information obtained is then used to construct a tailored mapping. (a) TT corresponding to JW encoding (b) Absolute values $|\theta_{ij}^{s}|$ after UpCCGSD, corresponding to single excitations between MOs i and j. (c) Absolute values $|\theta_{ij}^{d}|$ after UpCCGSD, corresponding to double excitations between MOs i and j. (d) Mutual information matrix between SOs for the JW ground-state. (e) Reordered mutual information matrix minimizing Eq. (16). (f) Constructed mapping encoding the most relevant double excitation subspace locally in parity. (g) Ground-state mutual information matrix for the adapted mapping that reduces entanglement on the double excitation between SOs 0, 1, 2, and 3. (h) Ground-state reordered mutual information matrix for the adapted mapping. Red labels indicate the cost function value of the corresponding mutual information matrices, and red squares indicate the four qubits directly involved in the most relevant double excitation.

To visualize the effects of the tailored mapping, we examine the MI matrix of the associated ground-state obtained by exact diagonalization [Fig. 3(g)]. In particular, we analyze the double excitation marked in red. Qubits A, B, C, and D defined in the idealized scenario from Eq. (7) correspond, respectively, to qubits 2, 3, 6, and 7 (marked by red squares). Notably, qubits B (3) and D (7) exhibit significant entanglement in accordance with Eq. (10), as indicated by the mutual information elements $I_{3,7} = I_{7,3}$. The same argument holds for the pink double
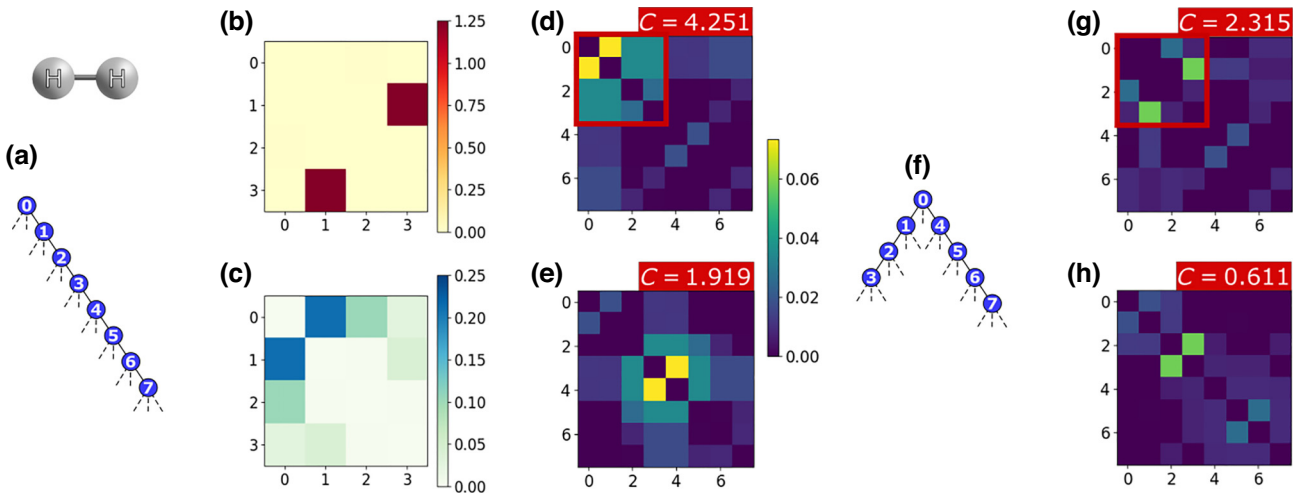

FIG. 9. Entanglement reduction process for H_2. Analogous to the benzene π system in Fig. 3. (a) JW mapping. (b) Absolute values $|\theta_{ij}^{s}|$ after UpCCGSD. (c) Absolute values $|\theta_{ij}^{d}|$ after UpCCGSD. (d) MI matrix between SOs for the JW ground-state. SOs involved in the most relevant double excitation are marked in the red square. (e) Reordered JW MI matrix minimizing Eq. (16). The cost function is indicated in red. (f) Tailored mapping proposed from the excitation analysis. (g) Ground-state MI matrix for the tailored mapping that simplifies entanglement on the qubits involved in the relevant double excitation (marked in the red square). (h) Ground-state reordered MI matrix for the tailored mapping. The cost function is indicated in red.
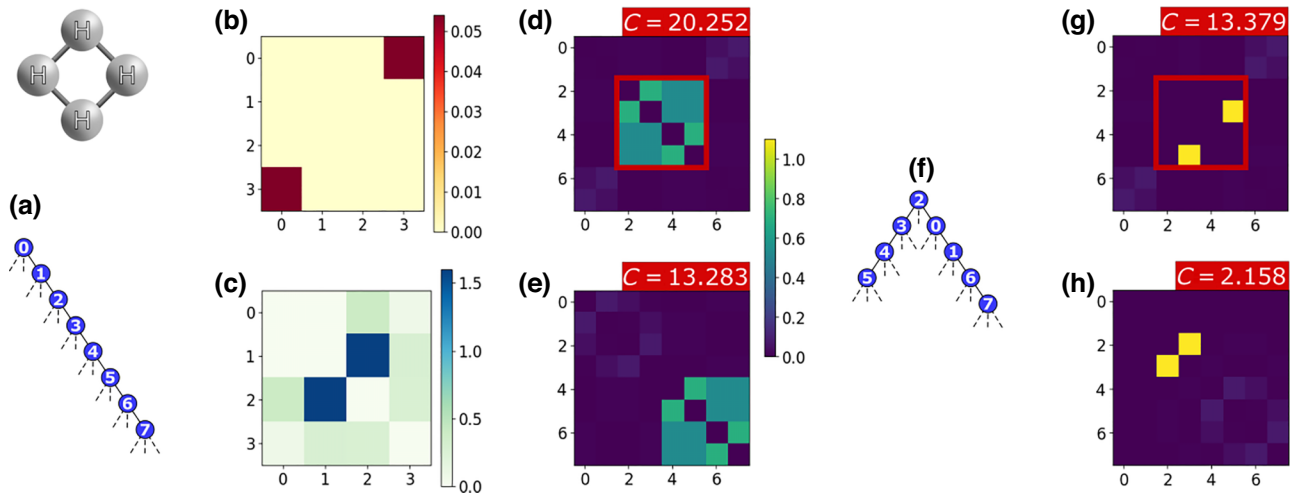
FIG. 10. Entanglement reduction process for square $H_4^{\neq}$. Analogous to the benzene π system in Fig. 3. (a) JW mapping. (b) Absolute values $|\theta_{ij}^s|$ after UpCCGSD. (c) Absolute values $|\theta_{ij}^d|$ after UpCCGSD. (d) MI matrix between SOs for the JW ground-state. SOs involved in the most relevant double excitation are marked in the red square. (e) Reordered JW MI matrix minimizing Eq. (16). The cost function is indicated in red. (f) Tailored mapping proposed from the excitation analysis. (g) Ground-state MI matrix for the tailored mapping that simplifies entanglement on the qubits involved in the relevant double excitation (marked in the red square). (h) Ground-state reordered MI matrix for the tailored mapping. The cost function is indicated in red.

excitation. While the transformation has simplified the entanglement structure, it is important to remark that not all qubits have been perfectly disentangled. This is due to additional single and double excitations contributing to the overall entanglement. Most importantly, the MI matrix for the new mapping can be now rearranged, minimizing the cost function from Eq. (16), yielding [Fig. 3(h)]. When we

compare the value of the cost function for the reordered tailored mapping ($C = 8.965$) with that of the JW mapping reordered matrix ($C = 19.632$), it becomes evident that we have achieved a significant reduction in correlation requirements.

This method was successfully applied to other small molecular systems (Figs. 8–11). For LiH, the method was
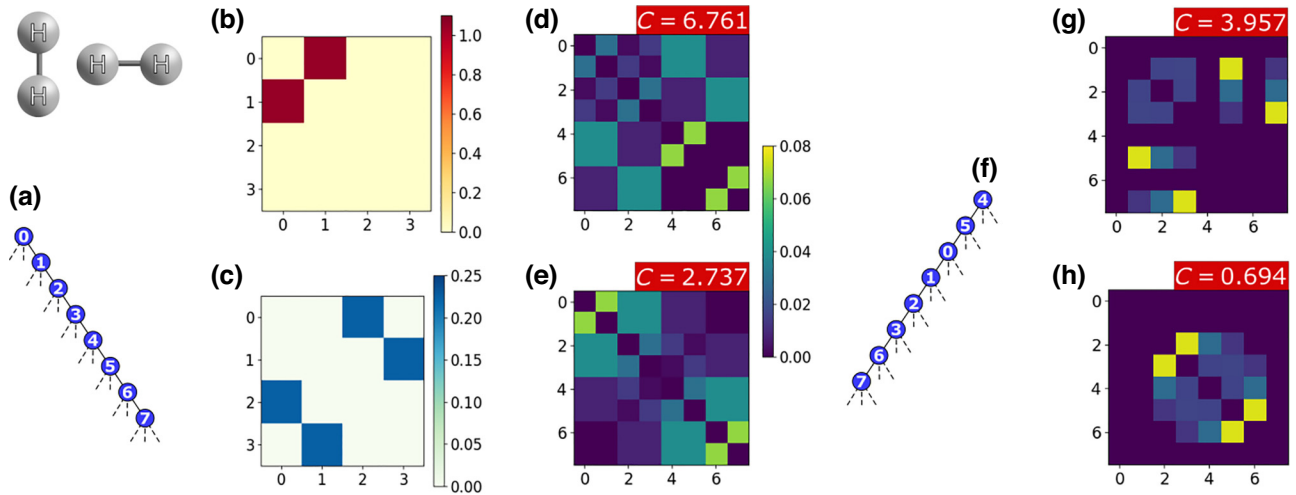

FIG. 11. Entanglement reduction process for $(H_2)_2$. Analogous to the benzene π system in Fig. 3. (a) JW mapping. (b) Absolute values $|\theta_{ij}^s|$ after UpCCGSD. (c) Absolute values $|\theta_{ij}^d|$ after UpCCGSD. (d) MI matrix between SOs for the JW ground-state. SOs involved in the most relevant double excitation are marked in the red square. (e) Reordered JW MI matrix minimizing Eq. (16). The cost function is indicated in red. (f) Tailored mapping proposed from the excitation analysis. Note that the two double excitations involving SOs (0, 1, 4, 5) and (2, 3, 6, 7) are included contiguously in the resulting parity order, on top of the (0, 1, 2, 3) SOs involved in the single excitation. (g) Ground-state MI matrix for the tailored mapping that simplifies entanglement on the qubits involved in the relevant double excitation (marked in the red square). (h) Ground-state reordered MI matrix for the tailored mapping. The cost function is indicated in red.
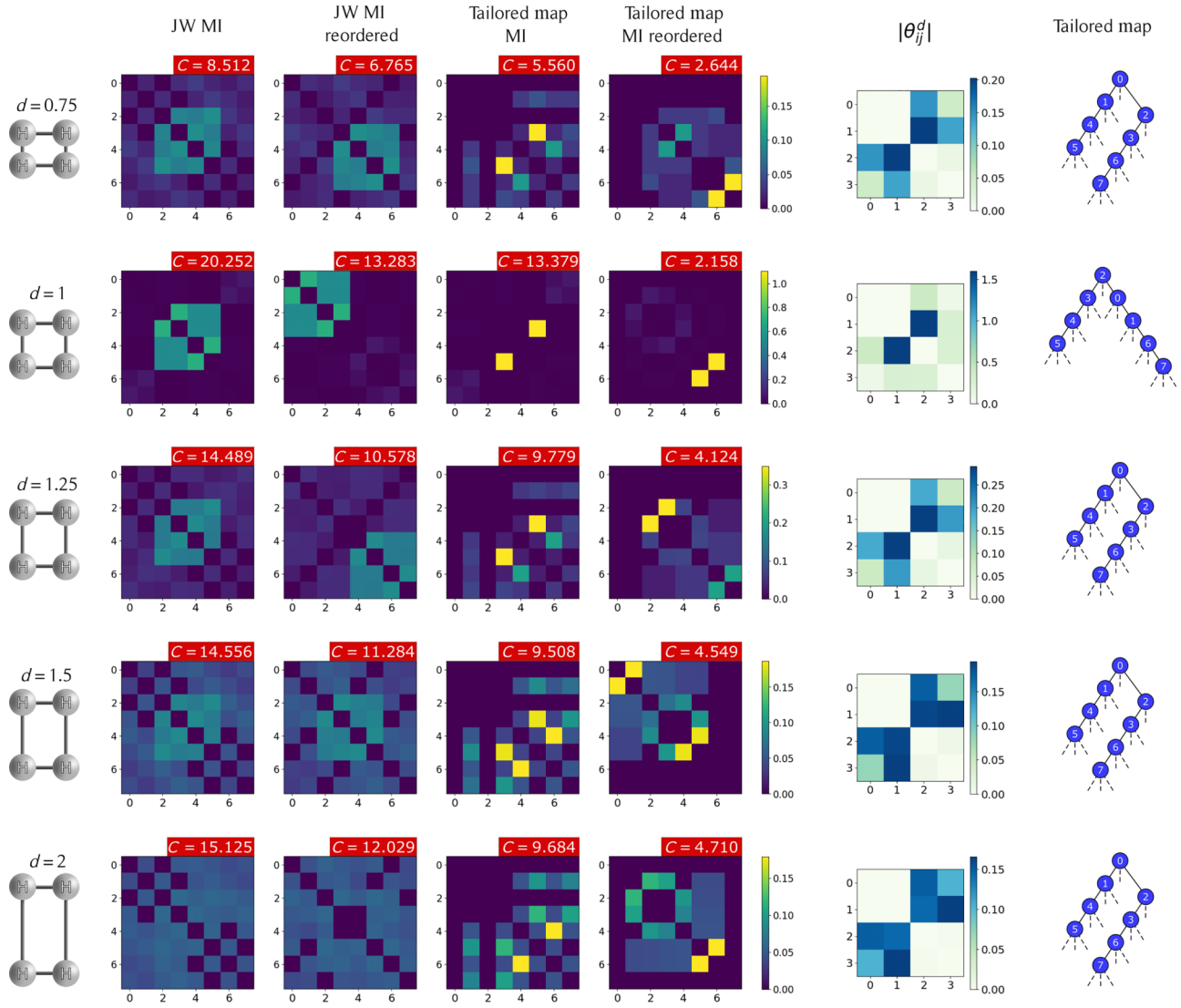
FIG. 12. Ground-state mutual information of the Paldus rectangle-to-square transition of $H_4^{\neq}$. Each row represents a distinct relationship d between side lengths, with a fixed horizontal length of 1.1203 Å. The first two columns depict the MI matrices of the JW map (unordered and reordered, respectively). The third and the fourth columns represent the MI matrices from the tailored map (unordered and reordered, respectively). The tailored map is built from the double excitation analysis for each case in the fifth column, and is explicitly shown in the last column. The cost function for each MI matrix is indicated in red. Single excitation angles are omitted from display as they hold reduced significance within the analyzed system.

used to disentangle the 0-4 double excitation. For H_2 in the 6-31G basis (four MOs), the 0-1 double excitation was simplified. In the case of the highly correlated $H_4^{\neq}$ square system, which also features four MOs and poses a four-electron problem, we used the same approach to simplify the double excitation involving MOs 1 and 2. In the scenario of $(H_2)_2$, we encountered two different double excitations, each involving distinct MOs. To tackle this situation, the decision protocol $\mathcal{D}$ was to select both excitations, which introduced a TT encoding scheme with a unique parity x branch encoding both excitations at the same time.

Additionally, a stretching analysis of the $H_4^{\neq}$ Paldus system was conducted (Fig. 12). The MI matrix was reconstructed for the exactly diagonalized ground-state across various configurations, ranging from rectangular to square ones. The stretching parameter d captures this variation. One side of $H_4^{\neq}$ is fixed at 1.1202 Å, while the other side is determined by our multiplying this fixed distance by the stretching parameter d. Across all cases explored, the tailored map yields a reduced value of the cost function, with both unordered and reordered qubits. For the square configuration ($d = 1$), a single excitation from the UpC-CGSD suggests the encoding of a parity branch spanning

spin-orbitals 2, 3, 4, and 5. Conversely, in other configurations, three relevant double excitations emerge, reflecting the rich entanglement patterns when canonical orbitals out of equilibrium are used. In this cases, we choose to encode the two double excitations from MOs 0 and 2, and from MOs 1 and 3, within distinct parity branches. Overall, our observations indicate that a suitable mapping may vary across different configurations, underscoring the importance of executing UpCCGSD for each configuration individually.

The use of canonical orbitals instead of localized atomic orbitals disrupts the connection between resonant structures and the tree structure of the mapping. This occurs because the tree structure is linked to the correlation between canonical orbitals, whereas resonant structures are associated with the correlation between localized orbitals centered on atomic nuclei. This is particularly evident in benzene: Kekulé resonant structures relate to localized electrons on the atoms, while canonical spin-orbitals delocalize electrons across the entire molecule. A similar phenomenon is observed in $H_4^{\neq}$, where the resonant structures of horizontal and vertical bonds do not correspond to the correlations of delocalized canonical orbitals.

It is important to emphasize that the use of MI as a post-analysis tool was introduced in previous work. Although it is a powerful tool, its use is not strictly necessary to observe the entanglement reduction resulting from our mappings. This is evident in any of the cases studied. The MI cost function value of the nonreordered ground-state for the tailored mapping [see, for instance, Fig. 3(g)] is smaller than that for the nonreordered JW mapping [Fig. 3(d)].

V. ENHANCING VQE PERFORMANCE

On the molecular Hamiltonians considered, VQE performance was evaluated for JW and tailored TT mappings. VQE simulations were implemented in TEQUILA with use of the COBYLA optimizer [49] and the QULACS simulator [50]. We compare the lowest VQE energy (E_{VQE}) obtained after ten VQE executions with the full CI (FCI) energy (E_{FCI}), with respect to the number of entangling layers used in an HEA consisting of RY gates. The RY HEA used consists of alternating layers of parameterized RY rotations and entangling controlled NOT gates (Fig. 13).

In Fig. 4, we display the VQE simulations for the π system of benzene [51]. The tailored mapping derived in the previous section shows enhanced performance with respect to JW mapping. With the JW approach, ten entangling layers on the RY HEA achieve a precision within 40 kcal/mol of the exact solution. In contrast, the tailored mapping achieves the same level of precision with only four entangling layers and offers even greater accuracy when expanded to ten layers.

VQE simulations for small molecular systems are shown in Fig. 14, including LiH, H_2, $(H_2)_2$, and square $H_4^{\neq}$; the benchmarked data for the JW mapping extracted from Ref. [47] are included. We conducted a replication of the method using our own hyperparameters and number of runs, both for the JW mapping and and for the tailored mapping derived in the previous section. Overall, the proposed mappings demonstrate superior performance across all systems studied, leading to faster attainment of chemical accuracy at 1 kcal/mol for the small molecules. For LiH, our tailored mapping achieves chemical accuracy with just four layers, in contrast to the eight layers required by the JW mapping. For the H_2 and $(H_2)_2$ cases, the selected mapping achieves accuracy with only six layers, whereas JW mapping fails to reach this level of precision even with ten layers. For the highly correlated $H_4^{\neq}$ square system ($E_{HF} - E_{FCI} = 153.640$ kcal/mol), chemical accuracy is attained with the tailored mapping with eight entangling layers, while the JW mapping falls short again when ten entangling layers are used.

In addition, the stretching of the Paldus $H_4^{\neq}$ system was simulated with use of the VQE for various values of the stretching parameter d and various numbers of RY-HEA entangling layers (Fig. 5). The tailored mappings, which differ for each stretching, are detailed in the correlation study for the Paldus system (Fig. 12). As we transition to nonequilibrium geometries (such as for $d = 2$), the significance of static correlations becomes evident, as demonstrated by the correlation analysis. However, the method proves to be efficient along the binding curve of $H_4^{\neq}$. When eight entangling layers are used, the tailored mappings accurately simulate any stretching up to chemical precision. In contrast, the JW mapping with an equivalent number of entangling layers fails to attain a similar level of precision.
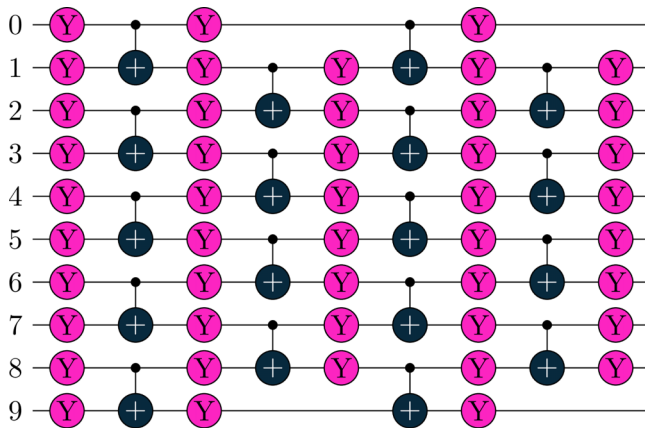

FIG. 13.   Example of parameterized RY HEA of four entangling layers, assembled from parameterized R_y rotations and static controlled NOT gates, used for the VQE optimization.
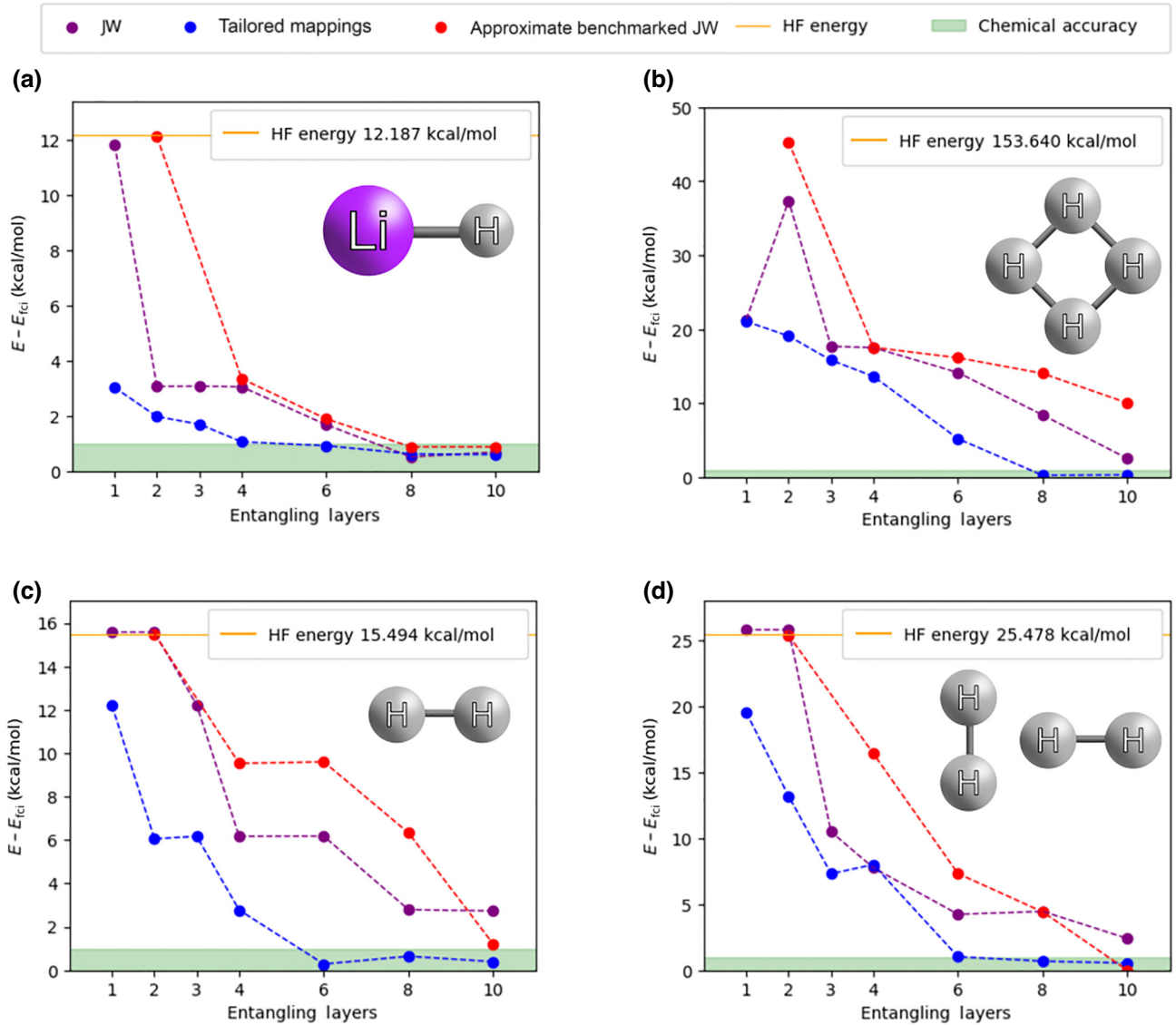
FIG. 14.　$E_{\mathrm{VQE}} - E_{\mathrm{FCI}}$ as a function of the number of RY-HEA entangling layers for the molecular systems of (a) LiH, (b) $H_4^{\neq}$, (c) H_2, and (d) $(H_2)_2$. Comparison of the benchmarked JW mapping with reordered qubits (red) in Ref [47], JW mapping with reordered qubits executed with our optimizers, backends, and hyperparameters for fair comparison (purple), and tailored mapping reordered (blue).

The motivation for using an RY-HEA primitive circuit design is to provide a balanced ground for comparisons between standard and tailored fermion-to-qubit mappings. When compared with targeted circuit designs in the JW representation [21], we reach competitive circuit depths (9 vs 12 for LiH, and 17 vs 130 for $H_4^{\neq}$). Note that by the design of the RY HEA, this comes with an increased parameter count (46 vs 5 for LiH, and 64 vs 10 for H_4) in addition to substantially greater iteration counts. Since the techniques from Ref. [21] do not strictly require a JW representation, we estimate significant improvements in combination with the fermion-to-qubit mappings developed in this work.

VI. ENHANCING DMRG PERFORMANCE

The method from the previous sections has direct applicability to tensor networks. To showcase this, we performed a DMRG optimization over a simple low-dimensional MPS ansatz using TeNPy [52]. The molecular system of N_2 was initialized in the STO-3G basis with two core orbitals frozen, resulting in an active space of 16 SOs (Table II). Again, a UpCCGSD optimization was performed, resulting in converged angles $\{|\theta_{ij}^s|\}$ and $\{|\theta_{ij}^d|\}$ for single excitations [Fig. 6(a)] and double excitations [Fig. 6(b)], respectively. We immediately appreciate the relevant contributions of double excitations between MOs 2 and 6 and between MOs 3 and 5, and

propose a TT mapping encoding such excitations in parity. In this case, we encode each double excitation in a different parity x branch of the TT, as depicted in Fig. 6(c).

Subsequently, a study using the DMRG was undertaken to assess the effectiveness of the proposed mapping. The energy obtained (E_{DMRG}) was compared with E_{FCI} for different maximum bond dimension cutoffs (χ_{max}), keeping for each bond dimension the best result after ten optimizations to avoid convergence of local minima [Fig. 6(d)]. For the DMRG, an exponentially decaying mixer was applied for 30 sweeps, allowing a maximum number of 500 sweeps for the optimization. Several scenarios were computed to study the dependency on χ_{max}. First, the best JW result was plotted in the standard spin-orbital ordering (red dots). Orbital reordering was then performed by our minimizing the cost function from Eq. (16) for the MI matrix, and the DMRG was executed again in the optimized order (red circles) [45]. The DMRG was also performed on our tailored mapping (blue dots), and the same reordering process was applied to permute the MPS sites and execute the DMRG again (blue circles).

An improvement of the DMRG performance is observed with the tailored TT mapping. For a given χ_{max}, the DMRG algorithm achieves lower converged energies, leading to a more accurate simulation of the quantum state. We relate such improvements to the reduced entanglement requirements. A decrease in block entropy is observed for the tailored mapping, in the cases of both standard ordering and reordered systems. This is visualized by our studying the block entropy for the best converged MPS at $\chi_{max} = 50$ [Fig. 6(e)]. The final MI matrices for the converged states at $\chi_{max} = 50$ are displayed in Fig. 15.

VII. OPTIMALITY

The algorithm presented is heuristic and based on an intuitive understanding of the role of excitations in the generation of correlations in fermion-to-qubit mappings. An enhanced performance is observed in the examples studied; however, it is not expected that our algorithm systematically provides the optimal mapping in terms of resources, say, the number of layers or bond dimension in the quantum and classical variational approaches considered, needed to obtain a given energy value. For H_2, we studied how our construction compares with other possible mappings. In particular, we sampled all possible tree structures, globally optimized over the mutual information with use of a brute force search of all permutations,
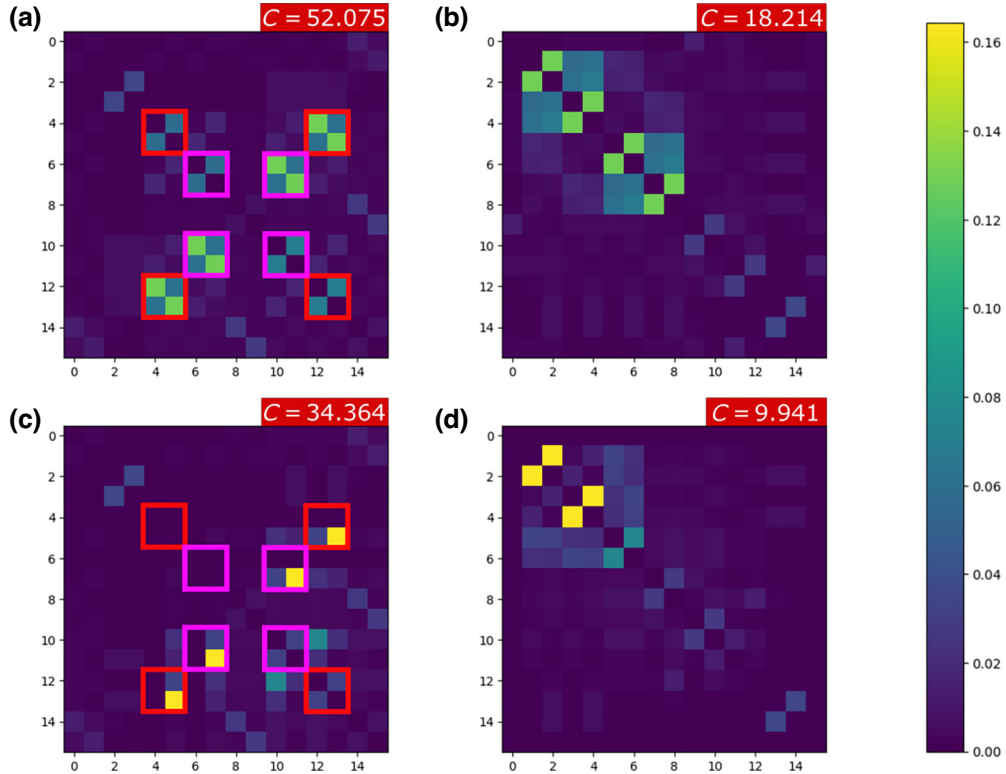

FIG. 15. N_2 MI matrices for the converged MPS after use of the DMRG for maximum bond dimension 50 in Fig. 6. The cost function is indicated in red. The qubits involved in the two relevant double excitations are marked in red and pink squares. (a) JW encoding. (b) JW with reordered qubits. (c) Constructed mapping after excitation analysis in Fig. 6(c). (d) The same constructed mapping reordered.
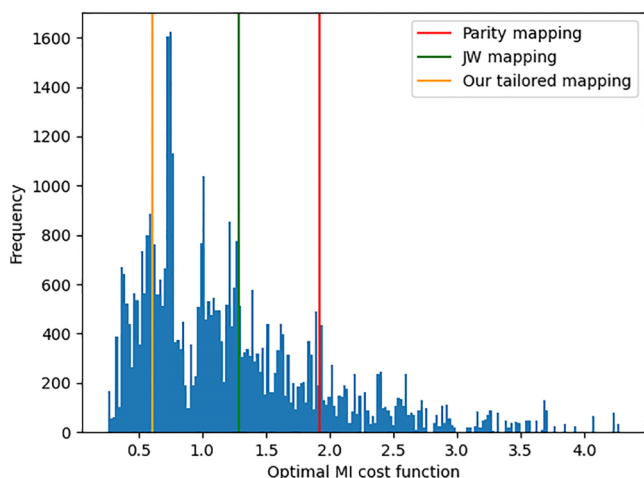
FIG. 16.   Distribution of MI cost function for the sampling of mappings for the H_2 molecule.

and then tested the resulting mapping with both the single-layer VQE and the double-layer VQE. For H_2, our tailored mapping has an optimal MI cost function of 0.611, versus the 1.28 of the JW mapping or the 1.92 of the parity mapping in standard orbital ordering. Of all the optimized MI of all tree shapes, our tailored mapping has lower MI than 81% of all mappings sampled (Fig. 16). This study also led to the discovery of trees with lower MI; however, each of these displayed worse performance than the tailored mapping when tested with the single-layer VQE and the double-layer VQE. Although the general trend was that lower MI correlates with better few-layer VQE performance, it is shown not to be guaranteed. It should be noted that this is a heavily restricted VQE, so perhaps it is not so surprising that random mappings do not suppress the four-body correlations sufficiently in order to be expressible in the fewer-than-four-layer VQE.

VIII. CONCLUSIONS

In this study we have introduced a novel physically inspired perspective in the design of fermion-to-qubit mappings. Previous efforts predominantly focused on reducing the average Pauli weight or the number of qubits used, which is undeniably important for quantum simulations. However, by focusing on the major sources of correlation in the physical problem, we have shown that transformations can be tailored in the qubit space to significantly simplify simulations. Our formalism can be used in both classical and quantum computing.

Our work points at several research directions that deserve further investigation. First, it remains to consider the extension of our results to higher-order fermionic excitations, on top of fermionic systems with larger spin number. Another critical aspect to investigate revolves

around the correlation-mitigating capabilities of our mappings, when scaling to larger systems is done. Additionally, it is important to note that our method reduces circuit depth while not focusing on the Pauli weight. This suggests that our method might manifest a greater Pauli weight in comparison with alternative composable low-depth TT mappings. Subsequent efforts could be focused on optimizing this aspect while simultaneously diminishing the entanglement. In the context of a noisy VQE, the question emerges of how advantageous can this trade-off be, which can be studied in future work.

Although in this work we used archetypal simulation methods, it remains to be seen how powerful a combination of inspired mappings with other ansatzes can be. That is, in the tensor network framework, more general ansatzes differing from the linear MPS could possibly benefit widely from the reduced entanglement. In the quantum computing framework, the simple but generic RY HEA was used for VQE simulations. The synergy of different ansatzes with our method could be studied. These could include not only the widely recognized adaptative family, but also other approaches informed by chemical valence-bond arguments [53]. Finally, while our formalism has been applied to electronic structure systems found in quantum chemistry, we anticipate possible adaptations of the method to fermionic systems of different nature, such as those found in nuclear structure or condensed matter simulations.

[1] N. S. Blunt, *et al.*, Perspective on the current state-of-the-art of quantum computing for drug discovery applications, J. Chem. Theory. Comput. **18**, 7001 (2022).

[2] Y. Cao, J. Romero, and A. Aspuru-Guzik, Potential of quantum computing for drug discovery, IBM J. Res. Dev. **62**, 6:1 (2018).

[3] V. von Burg, *et al.*, Quantum computing enhanced computational catalysis, Phys. Rev. Res. **3**, 033055 (2021).

[4] V. Lordi and J. M. Nichol, Advances and opportunities in materials science for scalable quantum computing, MRS Bull. **46**, 589 (2021).

[5] S. R. White, Density matrix formulation for quantum renormalization groups, Phys. Rev. Lett. **69**, 2863 (1992).

[6] U. Schollwöck, The density-matrix renormalization group, Rev. Mod. Phys. **77**, 259 (2005).

[7] G. K.-L. Chan and S. Sharma, The density matrix renormalization group in quantum chemistry, Annu. Rev. Phys. Chem. **62**, 465 (2011).

[8] M. R. Alberto Baiardi, The density matrix renormalization group in chemistry and molecular physics: Recent developments and new challenges, J. Chem. Phys. **152**, 040903 (2020).

[9] B. L. Hammond, W. A. Lester Jr, and P. J. Reynolds, *Monte Carlo Methods in ab Initio Quantum Chemistry* (World Scientific, Singapore, 1994).

[10] S. B. Bravyi and A. Y. Kitaev, Fermionic quantum computation, Ann. Phys. **298**, 210 (2002).

[11] A. Y. Vlasov, Clifford algebras, spin groups and qubit trees, Quanta **11**, 97 (2022).

[12] Z. Jiang, A. Kalev, W. Mruczkiewicz, and H. Neven, Optimal fermion-to-qubit mapping via ternary trees with applications to reduced quantum states learning, Quantum **4**, 276 (2020).

[13] M. Steudtner and S. Wehner, Fermion-to-qubit mappings with varying resource requirements for quantum simulation, New J. Phys. **20**, 063010 (2018).

[14] F. Verstraete and J. I. Cirac, Mapping local Hamiltonians of fermions to local Hamiltonians of spins, J. Stat. Mech.: Theory Exp. **2005**, P09012 (2005).

[15] C. Derby, J. Klassen, J. Bausch, and T. Cubitt, Compact fermion to qubit mappings, Phys. Rev. B **104**, 035118 (2021).

[16] R. W. Chien, S. Xue, T. S. Hardikar, K. Setia, and J. D. Whitfield, Analysis of superfast encoding performance for electronic structure simulations, Phys. Rev. A **100**, 032337 (2019).

[17] R. W. Chien and J. Klassen, Optimizing fermionic encodings for both Hamiltonian and hardware, arxiv: Quantum Physics, https://api.semanticscholar.org/CorpusID:252816051, arXiv:2210.05652.

[18] A. Miller, Z. Zimborás, S. Knecht, S. Maniscalco, and G. García-Pérez, Bonsai algorithm: Grow your own fermion-to-qubit mappings, PRX Quantum **4**, 030314 (2023).

[19] K. Mitarai, M. Negoro, M. Kitagawa, and K. Fujii, Quantum circuit learning, Phys. Rev. A **98**, 032309 (2018).

[20] I. O. Sokolov, *et al.*, Quantum orbital-optimized unitary coupled cluster methods in the strongly correlated regime: Can quantum algorithms outperform their classical equivalents?, J. Chem. Phys. **152**, 124107 (2020).

[21] J. S. Kottmann, Molecular quantum circuit design: A graph-based approach, Quantum **7**, 1073 (2023).

[22] M. Motta, *et al.*, Quantum simulation of electronic structure with a transcorrelated Hamiltonian: Improved accuracy with a smaller footprint on the quantum computer, Phys. Chem. Chem. Phys. **22**, 24270 (2020).

[23] S. McArdle and D. P. Tew, Improving the accuracy of quantum computational chemistry using the transcorrelated method, https://api.semanticscholar.org/CorpusID:219956739 arXiv: Quantum Physics (2020).

[24] P. Schleich, J. S. Kottmann, and A. Aspuru-Guzik, Improving the accuracy of the variational quantum eigensolver for molecular systems by the explicitly-correlated perturbative [2]$_{R12}$-correction, Phys. Chem. Chem. Phys. **24**, 13550 (2022).

[25] A. Kumar, *et al.*, Quantum simulation of molecular electronic states with a transcorrelated Hamiltonian: Higher accuracy with fewer qubits, J. Chem. Theory Comput. **18**, 5312 (2022).

[26] I. O. Sokolov, W. Dobrautz, H. Luo, A. Alavi, and I. Tavernelli, Orders of magnitude increased accuracy for quantum many-body problems on quantum computers via an exact transcorrelated method, Phys. Rev. Res. **5**, 023174 (2023).

[27] W. Dobrautz, *et al.*, Ab Initio transcorrelated method enabling accurate quantum chemistry on near-term quantum hardware, arXiv: Quantum Physics, https://api.semanticscholar.org/CorpusID:257353631, arXiv:2303.02007.

[28] H. Volkmann, R. Sathyanarayanan, A. Saenz, K. Jansen, and S. Kühn, A qubit-ADAPT implementation for H_2 molecules using an explicitly correlated basis, arXiv: Quantum Physics, https://api.semanticscholar.org/CorpusID:260886807, arXiv:2308.07259.

[29] M. T. Fishman and S. R. White, Compression of correlation matrices and an efficient method for forming matrix product states of fermionic Gaussian states, Phys. Rev. B **92**, 075132 (2015).

[30] C. Robin, M. J. Savage, and N. Pillet, Entanglement rearrangement in self-consistent nuclear structure calculations, Phys. Rev. C **103**, 034325 (2021).

[31] C. E. P. Robin and M. J. Savage, Quantum simulations in effective model spaces: Hamiltonian-learning variational quantum eigensolver using digital quantum computers and application to the Lipkin-Meshkov-Glick model, Phys. Rev. C **108**, 024313 (2023).

[32] S. M. Hengstenberg, C. E. P. Robin, and M. J. Savage, Multi-body entanglement and information rearrangement in nuclear many-body systems: A study of the Lipkin–Meshkov–Glick model, Eur. Phys. J. A **59**, 231 (2023).

[33] R. V. Mishmash, *et al.*, Hierarchical Clifford transformations to reduce entanglement in quantum chemistry wave functions, J. Chem. Theory Comput. **19**, 3194 (2023).

[34] P. Schleich et al., Partitioning quantum chemistry simulations with Clifford circuits, J. Chem. Theory Comput. **19**, 4952 (2023).

[35] Z.-X. Shang, M.-C. Chen, X. Yuan, C.-Y. Lu, and J.-W. Pan, Schrödinger-Heisenberg variational quantum algorithms, Phys. Rev. Lett. **131**, 060406 (2023).

[36] P. Jordan and E. Wigner, Über das Paulische Äquivalenzverbot, Z. Phys. **47**, 631 (1928).

[37] J. S. Kottmann, *et al.*, TEQUILA: A platform for rapid development of quantum algorithms, Quantum Sci. Technol. **6**, 024009 (2021).

[38] M. Chiew and S. Strelchuk, Discovering optimal fermion-qubit mappings through algorithmic enumeration, Quantum **7**, 1145 (2023).

[39] S. R. Langhoff and E. R. Davidson, Configuration interaction calculations on the nitrogen molecule, Int. J. Quantum Chem. **8**, 61 (1974).

[40] R. J. Bartlett and M. Musiał, Coupled-cluster theory in quantum chemistry, Rev. Mod. Phys. **79**, 291 (2007).

[41] A. Anand, *et al.*, A quantum computing view on unitary coupled cluster theory, Chem. Soc. Rev. **51**, 1659 (2022).

[42] J. S. Kottmann and F. Scala, Compact effective basis generation: Insights from interpretable circuit design, arXiv:

Quantum Physics, https://api.semanticscholar.org/Corpus ID:257050538, arXiv:2302.10660.

[43] H. R. Grimsley, S. E. Economou, E. Barnes, and N. J. Mayhall, An adaptive variational algorithm for exact molecular simulations on a quantum computer, Nat. Commun. **10**, 3007 (2019).

[44] J. Lee, W. J. Huggins, M. Head-Gordon, and K. B. Whaley, Generalized unitary coupled cluster wave functions for quantum computation, J. Chem. Theory Comput. **15**, 311 (2018).

[45] G. Barcza, Ö. Legeza, K. H. Marti, and M. Reiher, Quantum-information analysis of electronic states of different molecular structures, Phys. Rev. A **83**, 012508 (2011).

[46] R. Olivares-Amaya, *et al.*, The ab-initio density matrix renormalization group in practice, J. Chem. Phys. **142**, 034102 (2015).

[47] N. V. Tkachenko, *et al.*, Correlation-informed permutation of qubits for reducing ansatz depth in the variational quantum eigensolver, PRX Quantum **2**, 020337 (2021).

[48] F.-A. Fortin, F.-M. De Rainville, M.-A. Gardner, M. Parizeau, and C. Gagné, DEAP: Evolutionary algorithms made easy, J. Mach. Learn. Res. **13**, 2171 (2012).

[49] M. J. Powell, A view of algorithms for optimization without derivatives, Math. Today- Bull. Inst. Math. Appl. **43**, 170 (2007).

[50] Y. Suzuki, *et al.*, Qulacs: A fast and versatile quantum circuit simulator for research purpose, Quantum **5**, 559 (2021).

[51] W. Sennane, J.-P. Piquemal, and M. J. Rančić, Calculating the ground-state energy of benzene under spatial deformations with noisy quantum computing, Phys. Rev. A **107**, 012416 (2023).

[52] J. Hauschild and F. Pollmann, Efficient numerical simulations with tensor networks: Tensor Network Python (TeNPy), SciPost Phys. Lect. Notes **5**, 005 (2018).

[53] S. E. Ghasempouri, G. W. Dueck, and S. De Baerdemacker, Modular cluster circuits for the variational quantum eigensolver, J. Phys. Chem. A **127**, 8168 (2023).